ATLAS CONF Note

ATLAS-CONF-2022-005

14th March 2022

Search for Resonant $WZ \to \ell\nu\ell'\ell'$ Production in Proton-Proton Collisions at $\sqrt{s} = 13$ TeV with the ATLAS Detector

The ATLAS Collaboration

A search for a WZ resonance, in the fully leptonic final state (electrons and muons), is performed using 139 fb^{-1} of data collected at a center-of-mass energy of 13 TeV by the ATLAS detector at the Large Hadron Collider. The results are interpreted in terms of a singly-charged Higgs boson of the Georgi-Machacek model, produced by WZ-fusion, and of a Heavy Vector Triplet, with the resonance produced by WZ-fusion or the Drell-Yan process. No significant excess is observed over the Standard Model predictions and limits are set on the production cross-section times branching ratio as a function of the resonance mass for these processes.

1 Introduction

Searches for diboson resonances provide an essential test of theories of electroweak symmetry breaking beyond the Standard Model (BSM): new charged scalar diboson resonances arise in various models with an extended Higgs sector [1–3] and vector resonances are predicted in various BSM scenarios [4–10]. In this note, a search for a WZ resonance produced via either Drell-Yan or vector-boson fusion (VBF) is conducted in the fully leptonic decay channel $\ell\nu\ell\ell$ ($\ell = e$ or μ). The proton–proton collision data, with an integrated luminosity of 139 fb^{-1}, were collected by the ATLAS detector [11] at the Large Hadron Collider (LHC) at a center-of-mass energy of $\sqrt{s} = 13$ TeV.

In the Minimal Supersymmetric Standard Model the tree-level coupling of the charged Higgs boson to WZ is loop-induced [12], and therefore strongly suppressed compared to fermionic couplings. Tree-level coupling to massive vector bosons, however, is present in extensions of the Standard Model with higher-isospin scalar fields [13–15]. Here, the Georgi-Machacek (GM) model is used as a benchmark [16, 17]. It is not strongly constrained [18], as it preserves custodial symmetry, ensuring at tree level that the parameter $\rho = M_W^2/(M_Z^2 \cos^2\theta_W) = 1$. The GM model extends the Higgs sector of the Standard Model (SM) by including one real and one complex triplet. A parameter $\sin\theta_H$, representing the mixing of the vacuum expectation values, determines the contribution of the triplets to the masses of the W and Z bosons. The physical scalar states are organized into different custodial multiplets: a fiveplet ($H_5^{++}, H_5^{+}, H_5^{0}, H_5^{-}, H_5^{--}$) that is fermiophobic but couples to W and Z bosons, a triplet, and two singlets, one of which is identified as the 125 GeV SM-like Higgs boson. Single production of $H_5^{\pm}$ occurs by vector-boson fusion and, in this analysis, the assumption that the triplet states are heavier than the fiveplet scalars means that it can only decay to $W^{\pm}Z$. The cross-section is proportional to $\sin^2\theta_H$. The singly-charged members of this fiveplet are the object of the present search in the VBF channel.

Parameterized Lagrangians [19–21] incorporating a Heavy Vector Triplet (HVT) allow the interpretation of searches for vector resonances in a generic way. Here, a simplified phenomenological Lagrangian [20] is used. The new heavy vector resonance, W', couples to the Higgs field and longitudinally polarized SM gauge bosons by virtue of the equivalence theorem [22], and is parameterized by the product of parameters $g_V c_H$. It couples to the fermions via the combination $(g^2/g_V)c_F$, where g is the SM SU(2) gauge coupling. The parameter g_V represents the typical strength of the vector-boson interaction, while the parameters c_H and c_F are expected to be of the order of unity in most models. The vector-boson scattering process, $pp \to W'jj \to WZjj$, is only sensitive to the gauge boson coupling and, in this case, the benchmark model used to interpret the results assumes no coupling of the heavy vector resonance to fermions.

In nearly all the parameter space explored in the present analysis, for both benchmark models the intrinsic width of the resonance is below 4% , which is lower than the experimental resolution. Results are provided for the VBF and Drell-Yan production modes separately, neglecting possible signal leakage between them.

The present analysis extends searches for resonant WZ production with a fully leptonic final state, performed by ATLAS in Run 1 and Run 2 of the LHC using pp collision data at $\sqrt{s} = 8$ TeV [23] and $\sqrt{s} = 13$ TeV [24], with 20.3 fb^{-1} and 36 fb^{-1} of integrated luminosity, respectively. A search by the CMS Collaboration for a W' in an extended gauge model at $\sqrt{s} = 8$ TeV with 19.5 fb^{-1} of data has obtained a mass limit as a function of the assumed $W'WZ$ coupling. A more recent search [25] by the CMS Collaboration for a singly-charged and a doubly-charged Higgs boson produced via VBF and decaying respectively into WZ and WW in the fully leptonic mode, using an integrated luminosity of 137 fb^{-1}, has yielded limits on the coupling parameter of the GM model as a function of mass.

Recent results from searches of diboson resonances with different final states are summarized in Refs. [26–28]. The results from searches for heavy VV and VH resonances ($V = W$ or Z) based on Run 1 data and on Run 2 data in the fully hadronic ($qqqq$), semileptonic ($\ell\nu qq$, $\ell\ell qq$, $\nu\nu qq$), and fully leptonic ($\ell\ell\ell\ell$, $\ell\nu\ell\ell$, $\ell\ell\nu\nu$) final states are combined in Refs. [29–32]. The various decay channels generally differ in sensitivity in different mass regions. The present analysis, based on the fully leptonic channel, is particularly sensitive to low-mass resonances because of the low background, in spite of the low branching ratio. For the VBF process, it aims to complement previous explorations of the HVT phase space since other channels are mostly insensitive when the coupling of the heavy vectors to fermions is close to zero. Limits on the GM model have also been set, based on analyses of same-charge WW production and $WZjj$ by CMS [25, 33] and opposite-charge WW production by ATLAS [34], using data at $\sqrt{s} = 13$ TeV. In the present analysis, in addition to increased data statistics several improvements with respect to the previously published analysis have been implemented, most notably the implementation of multivariate techniques for the VBF signal selection.

2 The ATLAS Detector

The ATLAS detector [11] has a cylindrical geometry with a nearly 4π coverage in solid angle[1]. The inner detector (ID), consisting of silicon pixel, silicon microstrip and transition radiation detectors, is surrounded by a thin superconducting solenoid providing a 2 T axial magnetic field. It allows precise reconstruction of tracks from charged particles and measurement of their momenta up to a pseudorapidity of $|\eta| = 2.5$. High-granularity lead/liquid-argon (LAr) sampling electromagnetic and steel/scintillator-tile hadron calorimeters, at larger radius, provide energy measurements in the central pseudorapidity range $|\eta| < 1.7$. In the endcap and forward regions, LAr calorimeters for both the electromagnetic and hadronic energy measurements extend the region of angular acceptance up to $|\eta| = 4.9$. Outside the calorimeters, the muon spectrometer incorporates multiple layers of trigger and tracking chambers in a magnetic field produced by a system of superconducting toroid magnets, enabling an independent precise measurement of muon track momenta for $|\eta| < 2.7$. The ATLAS trigger system consists of a hardware-based level-1 trigger followed by a software-based high-level trigger [35]. An extensive software suite [36] is used in the reconstruction and analysis of real and simulated data, in detector operations, and in the trigger and data acquisition systems of the experiment.

3 Data and Monte Carlo Samples

The data, collected from 2015 to 2018 with the ATLAS detector in pp collisions at a center-of-mass energy of 13 TeV at the LHC, were selected by requiring that a set of quality criteria for detector and data conditions be satisfied [37].

Events are required to pass combinations of single-electron or single-muon triggers [38, 39]. The transverse momentum (p_{T}) threshold of the leptons in 2015 is 24 GeV for electrons and 20 GeV for muons satisfying a

---

[1] ATLAS uses a right-handed coordinate system with its origin at the nominal interaction point (IP) in the center of the detector and the z-axis along the beam pipe. The x-axis points from the IP to the center of the LHC ring, and the y-axis points upwards. Cylindrical coordinates (r, ϕ) are used in the transverse plane, ϕ being the azimuthal angle around the z-axis. The pseudorapidity is defined in terms of the polar angle θ as $\eta = -\ln\tan(\theta/2)$. Angular distance is measured in units of $\Delta R \equiv \sqrt{(\Delta\eta)^2 + (\Delta\phi)^2}$.

loose isolation requirement based only on ID track information. Due to the higher instantaneous luminosity in 2016-2018 the trigger threshold is increased to 26 GeV for both electrons and muons, and tighter isolation requirements are applied. Additional electron (muon) triggers that do not include any isolation requirements with p_{T} thresholds of 60 (50) GeV, and a single-electron trigger requiring $p_{\mathrm{T}} > 120$ GeV with less restrictive electron identification criteria are used to increase the selection efficiency which reached close to 100%, with respect to the offline selections. With these conditions, the integrated luminosity used in this analysis was 139 fb^{-1}.

Simulated signal events and background processes with prompt leptons are used to model the benchmark physics processes and optimize the selection cuts. They are produced by Monte Carlo (MC) generators with the detector response obtained from the GEANT4 toolkit [40, 41] integrated into the ATLAS simulation infrastructure. For some samples, the calorimeter response is obtained from a fast parametrized detector simulation [42], instead of full simulation by GEANT4. The effect of multiple interactions in the same and neighbouring bunch crossings (pile-up) was modelled by overlaying the simulated hard-scattering event with inelastic pp events generated with PYTHIA 8.186 [43] using the NNPDF2.3LO set of parton distribution functions (PDF) [44] and the A3 set of tuned parameters (tune) [45]. The distribution of the number of pileup events reproduces the bunch structure and the average number of interactions in the run periods. For all samples, except those generated with SHERPA [46], the EVTGEN 1.2.0 program [47] was used to simulate the properties of the b- and c-hadron decays.

The GM VBF benchmark signal samples, $pp \to H_5^{\pm}jj \to W^{\pm}Zjj \to \ell^{\pm}\nu\ell^{+}\ell^{-}jj$, vetoing W or Z bosons in the s-channel, are produced with MADGRAPH 2.7.2 [48] at next-to-leading order (NLO) in QCD, defined in Refs. [1, 49] for the mass range 200 GeV to 1 TeV in the H_5-plane defined in [1, 50], using the tool GMCALC [51]. The parameter $\sin\theta_H$ is set to 0.5 for masses up to 800 GeV and 0.25 for higher mass samples to be compatible with present constraints [50]. The matrix element calculation employed the `NNPDF30NLO` [52] set of PDFs. Events were interfaced to PYTHIA 8.186 for the modelling of the parton shower, hadronisation, and underlying event, using the A14 tuning parameters [53] and with the dipole recoil shower scheme to prevent the generation of an excess of central jet radiation [54]. For these samples, a minimum p_{T} of 15 GeV (10 GeV) for the jets (leptons) is required during event generation. The signal simulation is produced in 25 GeV mass steps up to 600 GeV and 100 GeV mass steps up to 1 TeV.

Two benchmark HVT production processes by Drell-Yan, $qq' \to W' \to WZ \to \ell\nu\ell\ell$, are used to interpret the results. Model A is typical of weakly coupled vector resonances arising from an extension of the SM gauge group [55] with an additional SU(2) symmetry, and the branching ratios to fermions and gauge bosons are comparable. Model B is representative of a HVT produced in a strongly-coupled scenario, as in a Composite Higgs model [56] with suppressed fermionic couplings. The parameter g_V is set to 1 for Model A and to 3 for Model B. For both models, c_F is set to 1 and is assumed to be the same for all types of fermions. The simulated signal samples for Model A are generated at leading order (LO) in QCD with MADGRAPH 2.6.5 using the model file provided by the authors of Ref. [20]. The parton-level simulated data are hadronized with PYTHIA 8.186, using the `NNPDF23_lo_as_0130_qed` PDF set and A14 hadronisation tune. The signal simulation is produced for masses of vector resonances ranging from 250 GeV to 5 TeV, in steps of 25 GeV below 600 GeV, 100 GeV between 600 GeV and 2 TeV, 200 GeV from 2 TeV to 3 TeV and 500 GeV above. For interpretation in terms of Model B, the Model A cross-sections are simply scaled. This is justified since the intrinsic resonance width remains well below the experimental resolution and the angular distributions are the same for both models.

For the VBF production mode of heavy vector resonances, which is expected to have a low cross-section, the benchmark model used is also based on the HVT parametrization. The coupling parameters g_V and c_H are set to 1 and all other couplings of the heavy triplet, including c_F, are set to 0 in order to maximize the VBF contribution. The simulated signal samples are generated at LO in QCD with MadGraph 2.6.5 using the model file provided by the authors of Ref. [20]. The parton-level simulated data are hadronized with Pythia 8.186, using the `NNPDF23_lo_as_0130_qed` PDF set and A14 hadronisation tune. A dijet invariant mass of at least 150 GeV is required in this case at event generation. The simulation samples are generated for masses ranging from 300 GeV to 2 TeV, in steps of 25 GeV (100 GeV) up to (beyond) 600 GeV.

The background sources include processes with two or more electroweak gauge bosons, namely VV and VVV ($V = Z, W$) as well as processes with top quarks, such as $t\bar{t}$, $t\bar{t}V$, and single top-quark, and processes with gauge bosons produced in association with jets or photons (V+j and $V\gamma$).

The dominant WZ SM background, here referred to as WZ-QCD, includes process up to order four in the electroweak coupling constant, α_{EW}, is modelled using Sherpa 2.2.2 [46]. The WZ production includes up to one jet calculated at NLO in QCD, while the second or third jet is calculated at LO in QCD and merged with the parton shower. In order to estimate an uncertainty due to generator and parton shower modelling, an alternative NLO WZ-QCD sample has been produced using MadGraph 5.2.6.5 with FxFx merging [57] of up to two extra jets. The hadronization is performed with Pythia 8.186. A sample of the purely electroweak process $WZjj \to \ell\nu\,\ell\ell\,jj$, including processes of order six in α_{EW} (WZ-EWK), was generated separately with MadGraph 2.7.3 together with Pythia 8.244. To estimate an uncertainty due to the parton shower modelling, a sample using the same matrix element and Herwig 7.2.1 for parton shower was produced. According to the SM a small interference occurs between electroweak and QCD WZ production. This is modelled using MadGraph 2.7.3+Pythia 8.244 and added together with the WZ-EWK simulation.

Samples of $q\bar{q} \to ZZ \to 4\ell$, $q\bar{q} \to ZZ \to \ell\ell\,\nu\nu$ and tribosons were generated with Sherpa 2.2.2 [58] using matrix elements at NLO accuracy in QCD for up to one additional parton and at LO accuracy for up to three additional parton emissions. The simulation included off-shell effects and Higgs boson contributions. The purely electroweak process $q\bar{q} \to ZZjj \to 4\ell jj$ and the $gg \to ZZ$ process are also generated with Sherpa 2.2.2 [58]. The LO-accurate matrix elements were matched to a parton shower based on Catani–Seymour dipole factorisation [59, 60] using the MEPS@LO prescription [61–64]. Samples were generated using the NNPDF3.0NNLO PDF set [52], and Sherpa parton-shower parameters.

The $t\bar{t}V$ processes were modelled using the MadGraph 2.3.3 [48] generator at NLO in QCD with the NNPDF3.0NLO [52] PDF. The events were interfaced to Pythia 8.210 [65] using the A14 tune and the NNPDF2.3LO [52] PDF set.

Finally, samples of SM backgrounds with at least one misidentified or non-prompt lepton, including $Z\gamma$, $W\gamma$, Drell–Yan $Z \to \ell\ell$, $W \to \ell\nu$ as well as top-quark pairs and single top-quark have been generated to assist in the fake/non-prompt lepton background estimate. Events with $V\gamma$ in the final state were simulated with the Sherpa 2.2.4 [58] generator. Matrix elements at LO accuracy in QCD for up to three additional parton emissions were matched and merged with the Sherpa parton shower [59–64]. The samples were generated using the NNPDF3.0NNLO PDF set [52], along with the dedicated set of tuned parton-shower parameters developed by the Sherpa authors. Drell–Yan $Z \to \ell\ell$ and $W \to \ell\nu$ are produced with Powheg Box v1 MC generator [66–69]. NLO accuracy was used for the hard-scattering processes of W and Z boson production and decay in the electron, muon, and τ-lepton channels. It was interfaced to Pythia 8.186 [43] for the modelling of the parton shower, hadronisation, and underlying event, with parameters set according to the AZNLO tune [70]. The CT10NLO PDF set [71] was used for the hard-scattering processes, whereas the CTEQ6L1 PDF set [72] was used for the parton shower. The effect of QED final-state radiation was simulated with Photos++ 3.52 [73, 74]. For top-quark pairs and single top-quark productions the

Powheg Box v2 [66–68, 75] generator at NLO with the NNPDF3.0NLO [52] PDF set was used. The events were interfaced with Pythia 8.230 [65] using the A14 tune [53] and the NNPDF2.3LO PDF set.

SM backgrounds with Higgs bosons ($H, t\bar{t}H, VH$) contribute less than 0.1% of the total background because of the low cross-section and the requirement of a well reconstructed Z boson decaying leptonically. These backgrounds are neglected.

4 Object Reconstruction and Identification

Electrons candidates are reconstructed from energy deposits in the electromagnetic calorimeter which are matched to a well-reconstructed ID track [76]. Only electrons with transverse energy E_{T} >7 GeV and within the pseudorapidity range of $|\eta|$ <2.47 and excluding the barrel-endcap transition region 1.37< $|\eta|$ <1.52 are considered.

Muons are either identified by matching muon spectrometer track with those in the ID or by using the calorimeter-based muon identification [77]. They are required to have transverse momentum p_{T} >5 GeV (p_{T} >15 GeV for calorimeter tagged) and pseudorapidity $|\eta|$ <2.7.

Identification and isolation criteria "loose", "medium" and "tight", as described in [76, 77], are applied to electron and muon candidates to suppress non-prompt leptons from hadron decays. Identification criteria are based on shower shapes and track parameters for electrons, and on track parameters for muons. The isolation criteria use information about ID tracks and calorimeter energy deposits in a fixed cone of $\Delta R = 0.2$ around each lepton. Four lepton categories are designed based on the identification and isolation criteria : *Baseline* electrons and muons are required to pass "loose" identification and isolation criteria (for muons with p_{T} >300 GeV the dedicated "High p_{T} identification" is required). The *Loose*, *Tight Z* and *Tight W* leptons are defined as subsets of the *Baseline* lepton selection with p_{T} >25 GeV. For the *Tight Z* leptons the "medium" identification and "tight" isolation criteria are required, while for *Tight W* leptons the "tight" identification and "tight" isolation criteria are required.

Electron and muon candidates are required to originate from the primary vertex. The primary vertex is defined, using tracks with p_{T} >500 MeV, as the vertex candidate with the highest $\sum p_{\mathrm{T}}^2$ of its associated tracks. The transverse impact parameter of the track (d_0) is calculated relative to the beam line. Thus, for all the four lepton categories, the longitudinal impact parameter, z_0 (the difference between the value of z of the point on the track at which d_0 is defined and the longitudinal position of the primary vertex), is required to satisfy $|z_0 \cdot \sin\theta|$ <0.5 mm. Furthermore, for the *Loose*, *Tight Z* and *Tight W* leptons the significance of the transverse impact parameter of the track, $|d_0/\sigma_{d_0}|$, must be smaller than 3.0 for muons and less than 5.0 for electrons.

Jets are based on particle-flow objects built from noise-suppressed positive-energy topological clusters in the calorimeter and reconstructed tracks [78]. The anti-k_t algorithm [79, 80] with a radius parameter of $R = 0.4$ is used.

For jets, the main backgrounds coming from collision events are beam-induced, due to proton collisions upstream of the interaction point, to cosmic-ray showers and to highly coherent calorimeter noise. These jets are considered “unclean” and rejected based on a set of quality criteria. Furthermore, to mitigate the pileup contamination, a jet vertex tagger [81, 82], based on information about tracks associated with the primary vertex and pileup vertices, is applied to jets with $p_{\mathrm{T}} < 60$ GeV and $|\eta| < 2.4$. In the forward region pileup jet tagging that exploits jet shapes and topological jet correlations in pileup interactions is applied to jets with $p_{\mathrm{T}} < 120$ GeV and $2.5 < \eta < 4.5$ [82].

The flavour of jets is determined using a deep-learning neural network, DL1r [83, 84]. The DL1r b-tagging is based on distinctive features of b-hadron decays in terms of the impact parameters of the tracks and the displaced vertices reconstructed in the inner detector. The b-tagging algorithm has an efficiency of 85% in simulated $t\bar{t}$ events, a light-flavour jet rejection factor of 33 and a c-jet rejection factor of about 3 [83].

Two levels of jet selections are used: the *Baseline* jets have $p_{\mathrm{T}} > 30$ GeV and $|\eta| < 4.5$, while for *VBF jets*, which are a subset of *Baseline* jets, the pileup removal using the jet vertex tagger and a b-tagging veto are applied, as described above.

To avoid cases where the detector response to a single physical object is reconstructed as two different final-state objects, an overlap-removal procedure is applied to the *Baseline* selected leptons and jets. If two electrons share the same track then the lower-p_{T} electron is discarded. Electrons that share the same track as a selected muon with a muon spectrometer track are also discarded; but in the case of a calorimeter-tagged muon, it is the muon which is rejected. A jet is removed if the separation from an electron satisfies $\Delta R < 0.2$; the electron is removed if the separation satisfies $0.2 < \Delta R < 0.4$. For nearly collinear muons and jets, the jet is removed if it is separated from the muon by $\Delta R < 0.2$ and if it has less than three tracks, or if the energy and momentum differences between the muon and the jet are small; otherwise the muon is removed if the separation satisfies $\Delta R < 0.4$.

The missing transverse momentum, $E_{\mathrm{T}}^{\mathrm{miss}}$, in an event is calculated as the magnitude of the negative vectorial sum of the transverse momenta of all *Baseline* selected and calibrated physics objects that can be matched to the primary vertex. A component called the "soft term" is calculated from the residual tracks that originate from the primary vertex but are not associated with any other object and is added to the $E_{\mathrm{T}}^{\mathrm{miss}}$ calculation [85].

5 Event Selection

In this search all final states with three charged leptons (electrons e or muons μ) and missing transverse momentum from WZ leptonic decays are considered. The search begins with a WZ baseline selection, and two selections are defined to build signal regions (SRs) targeting the Drell-Yan and VBF productions modes. A cut-based selection is used to build the Drell-Yan signal region, while for the VBF selection, an Artificial Neural Network (ANN) was trained. The invariant mass of the WZ candidates, $m(WZ)$, built with the leptons and $E_{\mathrm{T}}^{\mathrm{miss}}$ is used as discriminating variable. A summary of all the selections used to define the analysis regions can be found in Table 1.

5.1 Baseline selection of *WZ* events

The baseline selection is a set of event criteria applied to data and all simulated samples before defining more specific analysis regions. First, there is a requirement of good quality for the recorded events, based on the working conditions of all subdetectors. Events are vetoed if they have one or more unclean jets. All events are required to contain a primary vertex with at least two associated tracks.

Events are required to contain exactly three leptons passing the *Loose* selection criteria defined Section 4. In order to reduce the ZZ background, events with four or more leptons passing the *Baseline* criteria are

Table 1: Summary of the event selections for signal and control regions. Definitions of some variables used in this table can be found in Section 5.2 and 5.3.

<table>
<tr><th colspan="3">Baseline <i>WZ</i> selection</th></tr>
<tr><td colspan="3">Event cleaning and primary vertex
Single-electron or single-muon trigger
Exactly 3 <i>Loose</i> leptons (e or μ) with p_{T} >25 GeV(p_{T} >27 GeVfor trigger-matched lepton)
<i>ZZ</i> veto: veto events with additional <i>Baseline</i> leptons
Z candidate: A <i>Tight Z</i> Same-Flavour-Opposite-Sign lepton pair with $|m_{\ell\ell} - m_Z| < 20$ GeV
W candidate: <i>Tight W</i> lepton requirements on non Z leptons and $E_{\mathrm{T}}^{\mathrm{miss}} > 25$ GeV</td></tr>
<tr><td>Selection</td><td>Drell-Yan</td><td>VBF</td></tr>
<tr><td>Signal region</td><td>$p_{\mathrm{T}}(V)/m(WZ) > 0.35$</td><td>At least 2 <i>VBF jets</i>
$m_{jj} > 100$ GeV
Veto events with b-tagged jets
ANN Output > 0.82</td></tr>
<tr><td><i>WZ</i>-QCD control region</td><td>$p_{\mathrm{T}}(W)/m(WZ) \leq 0.35$ or
$p_{\mathrm{T}}(Z)/m(WZ) \leq 0.35$
$p_{\mathrm{T}}(V)/m(WZ) > 0.1$</td><td>At least 2 <i>VBF jets</i>
$m_{jj} > 500$ GeV
Veto events with b-tagged jets
ANN Output < 0.82</td></tr>
<tr><td><i>ZZ</i> control region</td><td>Additional <i>Baseline</i> lepton
No $E_{\mathrm{T}}^{\mathrm{miss}}$ requirement</td><td>Additional <i>Baseline</i> lepton
No $E_{\mathrm{T}}^{\mathrm{miss}}$ requirement
At least 2 <i>VBF jets</i></td></tr>
</table>

vetoed. To ensure that the trigger efficiency is well determined, at least one of the three candidate leptons must be trigger-matched and is required to have p_{T} >27 GeV. A Z candidate must be present. It is defined by two leptons of the same flavour and opposite charge with an invariant mass that is consistent with the Z boson pole mass (m_Z): $|m_{\ell\ell} - m_Z| < 20$ GeV. If there is more than one pair of leptons that can form a Z candidate, the one with invariant mass closest to the Z boson pole mass is chosen. The third lepton is then taken as the W boson lepton candidate. The leptons assigned to the W and Z candidates are then required to satisfy the *Tight W* or *Tight Z* selection criteria defined in Section 4. The tighter selection applied to the leptons of the W candidate is motivated by lower background rates in leptons from the Z candidate, which are well constrained by the requirement on their invariant mass. Finally, the missing transverse energy in the event is required to be greater than 25 GeV.

To reconstruct the four-vector of the W boson, the $E_{\mathrm{T}}^{\mathrm{miss}}$ of the event is assumed to be due to the neutrino. The longitudinal component $p_z(\nu)$ of the neutrino momentum is derived by constraining the invariant $\ell\nu$ mass to be the pole mass of the W boson, where the charged lepton is the one assigned to the W candidate. A quadratic equation leads to two solutions. If they are real, the one with the smaller magnitude of $|p_z(\nu)|$ is chosen, otherwise, the real part is chosen. The invariant mass of the WZ system is then calculated.

5.2 Drell-Yan process selection

For a heavy resonance produced essentially at rest in the s-channel, it is expected that the selected W and Z bosons have transverse momenta close to 50% of the resonance mass. The boson p_{T} to resonance mass ratio variable is therefore defined as the ratio $p_T^V/m(WZ)$ of the boson transverse momentum to the WZ invariant mass. To reduce the contribution of the non resonant WZ production, events passing the WZ preselection are required to have a boson p_T to resonance mass ratio greater than 0.35 for both bosons. The combined detector acceptance and signal selection efficiency ($A \times \epsilon$) of the Drell-Yan HVT W' selection, relative to the generated signal events, is shown in Figure 1. There, decays of W and Z bosons into all flavours of leptons are included at event generation. The $A \times \epsilon$ values decrease for resonance masses above approximately 2 TeV due to the collinearity of electrons from highly boosted $Z \rightarrow ee$ decays, for which the lepton isolation is less efficient.

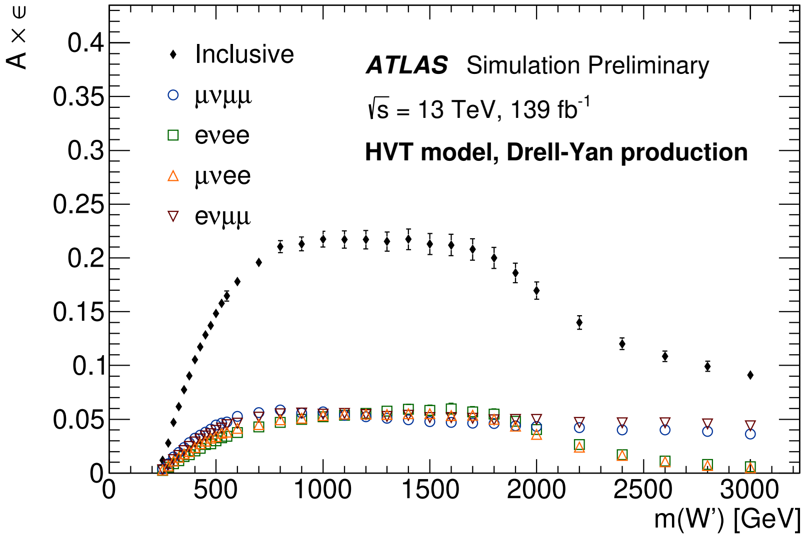

Figure 1: The acceptance (A) times efficiency (ϵ) of W' boson selection after the Drell-Yan signal region selection at different mass points for the individual channels $\mu\nu\mu\mu$, $evee$, μvee, $ev\mu\mu$, and the sum of all channels. The uncertainty includes both statistical and experimental systematic components.

5.3 Vector Boson Fusion process selection

The VBF process ($pp \rightarrow W'jj \rightarrow WZjj$) is characterized by the presence of two jets with a large rapidity gap resulting from quarks from which a vector boson has been radiated. To select the signal events, an Artificial Neural Network (ANN) with a binary classification task is used: events are categorized as belonging either to a VBF process or to the background. The ANN training is implemented using the Keras package [86] running on top of the TensorFlow package [87]. The ANN training region is defined by requiring events to have at least a pair of jets satisfying the *VBF jets* selection, and from those, the pair the highest-p_T jet is required to have an invariant (m_{jj} >100 GeV). The ANN is trained in this region with simulated $H_5^\pm$ events as signal, against the SM WZ EWK and QCD events as background. The $H_5^\pm$ simulation is used for the training as the kinematic variables show very similar distributions for both GM and HVT benchmark signals and the training yielded similar results.

In order to make use of the full statistics, a 4-fold cross-validation technique has been applied. The rectified linear unit, or ReLU, is used as an activation function at each node. The space of hyperparameters was scanned and a final set was chosen to ensure optimal performance of the network. The training was performed with 100 epochs, Nesterov's momentum 0.7 [88], two hidden layers of 45 neurons each. To avoid overfitting, a regularisation technique was employed. For each input sample, a hidden layer was randomly removed with probability parameter (dropout) of 0.2, allowing for a noisy training process. The distributions of loss function and accuracy vs epochs were monitored for the training and validations sets and no sign of overtraining was observed.

The list of the input variables used for the ANN optimization is given in Table 2. These were chosen on the basis of their impact in the training and such that highly correlated variables are not used simultaneously. The loss in expected significance by adding or exchanging some of the variables was evaluated for each set of variables until the optimal set was found.

All the mass samples of simulated $H_5^{\pm}$ GM events are used simultaneously for the training. After training, the cut value on the ANN output score is chosen in such a way that it maximizes the significance for the lowest mass point (200 GeV). The advantage of this approach is that it reduces considerably the training effort and a single signal region can be used. It was verified that the alternative of using one ANN training per mass point does not improve significantly the performance. The training is then applied to both GM and HVT Model samples. A minimum value of 0.82 on the ANN output maximizes the significance and is chosen to define the signal region. After all selection cuts are applied the VBF signal region effectively starts at $m_{jj} > 500$ GeV. This signal region was blinded until the background and its uncertainties in the control regions had been evaluated (Section 6).

Table 2: Variables used for ANN training.

Training variable	Definition
$\boldsymbol{m_{jj}}$	Invariant mass of the two leading-p_{T} jets
$\boldsymbol{\Delta\phi_{jj}}$	Difference in ϕ of the two leading-p_{T} jets
$\boldsymbol{\eta_W, \eta_Z}$	Pseudorapidities of the reconstructed gauge bosons
$\boldsymbol{\eta_{j1}}$	Leading-p_{T} jet pseudorapidity
$\boldsymbol{\zeta_{\mathrm{Lep}}}$	Event centrality[2]
$\boldsymbol{E_{\mathrm{T}}^{\mathrm{miss}}}$	Missing transverse energy
$\boldsymbol{H_T}$	Scalar p_{T} sum of the *VBF jets* and the leptons from the *WZ* decay

Good modelling by MC simulations of the distribution shapes and the correlations of all input variables to the ANN is verified in the *WZ*-QCD control region (see Section 6 for definition), and is exemplified by the good description of the ANN score distribution of data in the *WZ*-QCD control region and VBF signal region shown in Figure 2.

The acceptance times efficiency $\mathcal{A} \times \epsilon$ of the ANN-based VBF selection as a function of the mass of the VBF $H_5^{\pm}$ and of the HVT W' boson, relative to the generated signal events, are shown in Figure 3. There, decays of W and Z bosons into all flavours of leptons are included at event generation. For $H_5^{\pm}$ and the HVT boson the $\mathcal{A} \times \epsilon$ falls in the range 2–12% and 2–5% respectively for resonance masses ranging

---

[2] The "event centrality" is a measure of the smaller pseudorapidity difference between the most forward jet and the most forward lepton in either hemisphere. It is defined as:

$$\zeta_{\mathrm{Lep}} = \min\left\{\left[\min(\eta_{\ell_1}, \eta_{\ell_2}, \eta_{\ell_3}) - \min(\eta_{j_1}, \eta_{j_2})\right], \left[\max(\eta_{j_1}, \eta_{j_2}) - \max(\eta_{\ell_1}, \eta_{\ell_2}, \eta_{\ell_3})\right]\right\},$$

with ℓ_1, ℓ_2, ℓ_3 being the three leptons from the *WZ* decay and η_{j_1}, η_{j_2} the leading-p_{T} and subleading-p_{T} VBF jets.

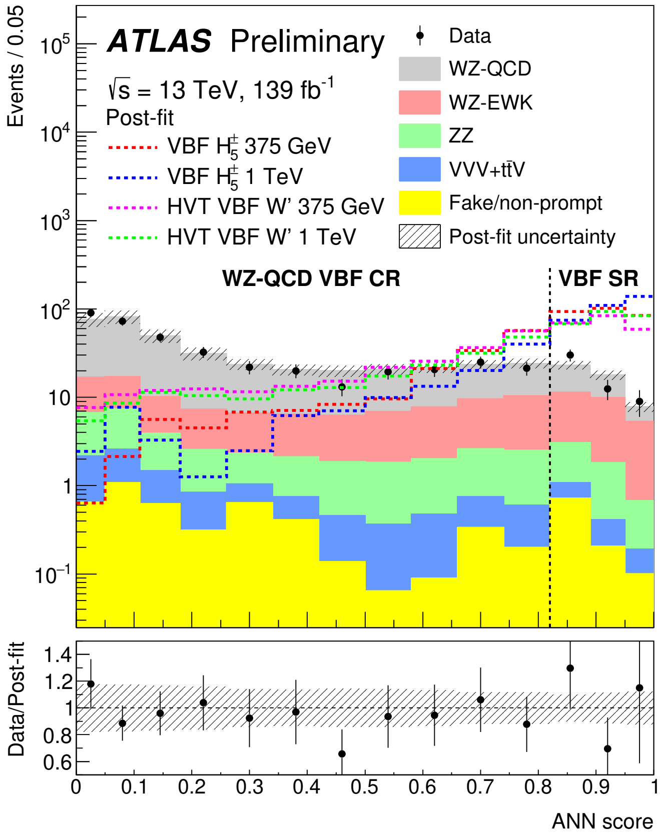

Figure 2: Distribution of the ANN discriminant output in the *WZ*-QCD VBF control region and the VBF signal region. The background predictions are obtained through a background-only simultaneous fit to the VBF signal region and the *WZ*-QCD VBF and *ZZ* VBF control regions as described in Section 8. The uncertainty in the total background prediction, shown as grey bands, combines statistical and systematic contributions. The distributions for the HVT VBF model W' and GM $H_5^\pm$ simulations are shown normalized to the data integral. The vertical dotted line shows the cut on the ANN output score used to define the VBF signal region.

between 200-1 000 GeV, the difference being due, with approximately equal importance, to the generator level selection and to the different angular distributions of the final products.

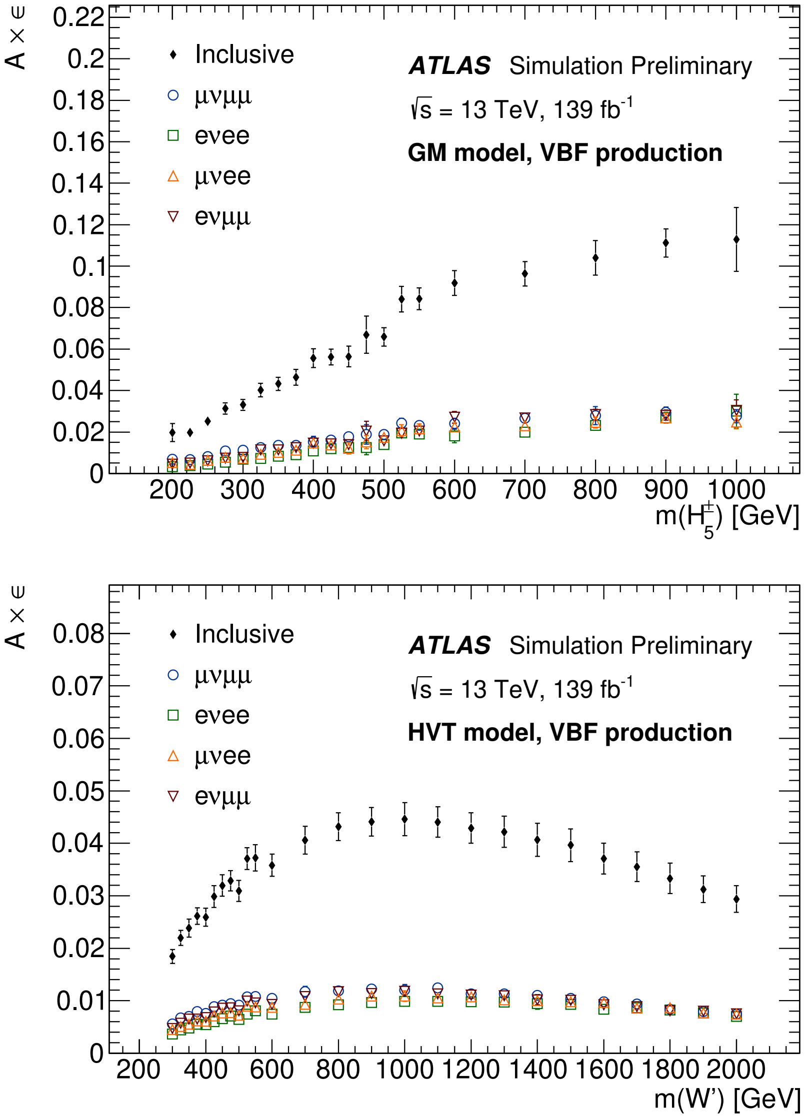

Figure 3: The acceptance (A) times efficiency (ϵ) of VBF $H_5^\pm$ (top) and HVT W' (bottom) selection after the ANN-based VBF selection at different mass points for the individual channels $\mu\nu\mu\mu$, $evee$, μvee, $e\nu\mu\mu$, and the sum of all channels. The uncertainty includes both statistical and experimental systematic components.

6 Background Estimation

The background sources are classified into two groups: the irreducible backgrounds where all reconstructed lepton candidates are prompt (arise from the primary process) and the reducible backgrounds where at least one of the lepton candidates is not prompt. Non-prompt leptons are also referred to as "fake/non-prompt" leptons.

The contributions from the irreducible backgrounds *WZ*-QCD, *WZ*-EWK, *ZZ*, *VVV* and $t\bar{t}V$ are estimated using MC simulation. The normalization of the *WZ*-QCD and *ZZ* is constrained by data in a simultaneous fit using the signal region and dedicated control regions (CRs). Each signal region is associated to two CRs that are designed to match their respective event topology and jet multiplicity, as summarized in Table 1.

The dominant source of irreducible background originates from the QCD mediated production of *WZ* dibosons. Two CRs are created to constrain it. One is referred to as *WZ*-QCD DY CR and is dedicated to the Drell-Yan analysis: it is defined by selecting the sub-sample of *WZ* events that fulfills all the Drell-Yan event selection but fails the boson p_{T} to resonance mass ratio. The minimum requirement of the boson p_{T} to resonance mass ratio is set to 0.1 in order to be close to the signal region. The second region, referred to as the *WZ*-QCD VBF CR, is dedicated to the VBF analyses. It is defined by selecting in the sub-sample of *WZjj* the events that fail the ANN score requirement, and have $m_{jj} > 500$ GeV. The high m_{jj} requirement is applied in order to match the signal region event topology. In both regions the *WZ*-QCD contributions is around 80%.

To extract the *ZZ* background normalization, two *ZZ*-enriched control regions are defined after applying the *WZ* event preselection described in Section 5.1. The presence of at least a fourth lepton candidate passing the *Baseline* identification criteria is required and no requirement on the missing transverse energy is applied. This region is used for the Drell-Yan process analysis and is referred to as the *ZZ* DY CR. For the VBF selection, the events in the *ZZ* VBF CR must have, in addition, at least two VBF tagged jets. The QCD mediated production of *ZZ* events represent 91% (80%) of the *ZZ* DY CR (*ZZ* VBF CR), while the contribution of electroweak mediated production *ZZ* events is small, we will refer in the following to the sum of both components as *ZZ* background.

To validate the modelling of the $t\bar{t}V$ background a dedicated validation region is built by requiring the *WZjj* events to have at least one b-tagged jet. Since no significant data mis-modelling was observed, the $m(WZ)$ shape and normalization of this background are taken from simulation.

The reducible backgrounds originating from Z+j, $Z\gamma$, $t\bar{t}$, *Wt* and *WW* processes where jets or photons were misidentified as leptons. For both analysis regions the reducible backgrounds normalizations are estimated using a data-driven method. The method is based in a global matrix which exploits the differences in object characteristics between real and fake/non-prompt leptons on a statistical basis. Details of the method can be found in Ref. [89] . The shape in the Drell-Yan analysis is obtained from the data-driven method. In the case of the VBF analysis, due to the limited statistics, the shapes are taken from simulation.

7 Systematic Uncertainties

Systematic uncertainties from the theoretical modelling, object and event reconstruction have an impact in the signal and control regions used. The search sensitivity is then affected by their effects on background estimations, signal acceptance, and the shape of the distributions of the invariant mass discriminant used. Depending on the nature of the uncertainty these can be classified into two groups: (a) theoretical uncertainties associated with the MC modelling of both the background and signal processes and (b) experimental uncertainties related to the detector and reconstruction performance. The uncertainties and the methods used to evaluate them are discussed below. Unless explicitly stated, the uncertainties quoted are the uncertainties in the quantities themselves, not their impact on the search sensitivity.

7.1 Theory uncertainties

Systematic uncertainties in the theoretical modelling by the event generators used to evaluate the WZ−QCD, WZ−EWK and ZZ templates are considered. For the WZ−QCD and ZZ backgrounds that have data-driven normalizations only the shape variations on the reconstructed $m(WZ)$ are considered. Uncertainties due to higher order QCD corrections are evaluated by varying the renormalisation and factorisation scales independently by factors of two and one-half. For the WZ−QCD background only a small shape effect is observed and used in the fit. For the WZ−EWK background the uncertainties grow with the mass from 8% up to 15% on the $m(WZ)$ shape. The uncertainties due to the PDF and the α_s value used in the PDF determination are evaluated using the PDF4LHC prescription [90]. For the WZ−QCD background they are estimated to have a small shape component but are nevertheless included in the fit, for the WZ−EWK they are added in quadrature, and the total uncertainty stays between 5 to 6% in all mass bins for both the Drell-Yan and VBF selections. A modelling uncertainty in the WZ-QCD background template that includes effects of the parton shower model is estimated by comparing predictions of the $m(WZ)$ distribution from the Sherpa and MadGraph MC generators. The difference between the predicted shapes of the distribution from the two generators is centered around the nominal prediction and considered as an uncertainty. A parton shower modelling uncertainty in the WZ-EWK background template is estimated using two MC samples with different parton shower models, Pythia and Herwig. This modelling uncertainty has no effect in the normalization at low mass but grows with the $m(WZ)$ distribution reaching 5% at high mass. For the ZZ background the shape uncertainties originating from the renormalisation and factorisation scales, as well as from PDF and the α_s are evaluated in a similar way. The theory uncertainties described above are evaluated in all the analysis signal and control regions and they are considered as uncorrelated across those regions in the statistical analysis.

An uncertainty of 20% is assigned to the $t\bar{t}V$ and VVV cross-sections [91–93]. It consists of contributions from PDF uncertainties and QCD scale uncertainties.

Uncertainties in the signal acceptances due to PDF and scale choices are also evaluated. These uncertainties are calculated following the procedure described above, for several resonant mass points, and for each model, production process and decay. The theory uncertainties on the HVT signals are evaluated to be under 20% for all production modes and they are 30% for the GM model.

7.2 Experimental uncertainties

Experimental uncertainties arise from the luminosity calculation, triggers, and reconstruction and identification of leptons and jets, as well as the computation of the missing transverse energy.

The uncertainty in the integrated luminosity is 1.7%. It is derived following a methodology similar to that detailed in Ref. [94] and using the LUCID-2 detector for the baseline luminosity measurements [95], from a calibration of the luminosity scale using x-y beam-separation scans. A variation in the pileup re-weighting of MC events is included to cover the uncertainty in the ratio of the predicted and measured inelastic cross-sections [96].

Systematic uncertainties affecting the reconstruction and energy calibration of jets are propagated through the analysis. They are the dominant experimental uncertainties in the VBF selection. Those due to the jet energy scale and resolution are obtained from simulations and *in-situ* techniques [97]. The uncertainties in the b-tagging efficiency and the mistag rate are also taken into account. The effect of jet uncertainties on the expected number of events ranges up to 15% in the VBF selection.

Uncertainties in the efficiencies of lepton triggers are found to be negligible. The uncertainties due to the electrons and muons reconstruction, identification and isolation requirements are estimated using tag-and-probe methods in $Z \to \ell\ell$ events in data and simulation [76, 77]. Uncertainties in the leptons energy scale and resolution are also assessed. The impact of lepton uncertainties on the expected number of events is typically below 1%.

The uncertainty in the missing transverse momentum measurement is estimated by propagating the uncertainties in the transverse momenta of preselected leptons and jets as well as those in the soft term [85].

An uncertainty in the prediction of the fake/non-prompt background is also taken into account as it affects the shape and normalization of the background distributions. The total uncertainty is about 60% (more than 100%) for the Drell-Yan (VBF) selections. It is larger for the VBF selection because of the higher statistical uncertainty.

8 Results

8.1 Statistical analysis strategy

The WZ invariant mass distribution, $m(WZ)$, is used as the discriminating variable, the bin widths were chosen to be comparable to the expected resolution of the resonant model under investigation, and at the same time to optimize the sensitivity of the search while reducing the impact of statistical fluctuations.

A profile-likelihood-ratio test statistic [98] is used to test the compatibility of the background-only hypothesis with the data and to test the signal-plus-background hypothesis. The binned likelihood function is constructed by considering, in each bin, the contributions of the backgrounds and of a hypothetical signal of given strength relative to a benchmark model production cross-section. In the absence of an observed signal, exclusion limits on the presence of a signal are then derived using the CLs method [99].

Maximum-likelihood fits are performed to the observed binned distributions of $m(WZ)$ in the signal regions and their dedicated WZ and ZZ control regions simultaneously. Separate fits are performed for the Drell-Yan and VBF selections. The normalization of the WZ-QCD and ZZ contributions are free floating parameters in these fits and are constrained by the data in both the SRs and dedicated CRs. The ratio of the fitted contributions in the CR and SR is allow to vary within the theory uncertainties. The normalization and shape of all other backgrounds are allowed to vary within their uncertainties.

Systematic uncertainties, described in Section 7, and their correlations are incorporated as constraints into the likelihood calculations through nuisance parameters, where each is given a Gaussian prior. Most of the systematic uncertainties are taken as correlated between the SR and CRs and constrained simultaneously in these regions, with the theory uncertainties on the ZZ, WZ-QCD and WZ-EWK backgrounds being the only exceptions.

Two fit configurations are used, referred to as the Drell-Yan and VBF configurations. The Drell-Yan fits include the Drell-Yan SR, WZ-QCD CR and ZZ-CR. In the VBF configuration, fits include the VBF-SR, $WZjj$-QCD CR and $ZZjj$-CR. Separate fits are performed for the different models tested and for different resonance mass hypotheses. The Drell-Yan configuration is used to search for a W' boson predicted by the HVT model. Two VBF-fits are performed using the VBF configuration: one for the search for a VBF produced W' predicted by the HVT model, and the second fit for the charged Higgs boson, $H_5^\pm$, search as predicted by the GM model.

8.2 Data and background comparisons

To test the compatibility of the data and the background expectations, the data are first fit to the background-only hypothesis, in both the Drell-Yan and VBF configurations.

The post-fit background yields are summarized in Table 3 for the Drell-Yan and VBF signal regions. The fit in both cases is able to adjust the SM ZZ and WZ-QCD background normalization using the data in signal and control regions. In the Drell-Yan fit, the ZZ background normalization is increased by around 10% while the WZ-QCD background is decreased by 10% with respect to the pre-fit predictions. Some mild pulls in the modelling uncertainties by less than one standard deviation from their pre-fit values are visible in the Drell-Yan fit. In the VBF fits, the normalization of the ZZ background is consistent with the pre-fit value while the WZ-QCD background is reduced by around 30%. Apart from the mild pulls in the Drell-Yan signal region, none of the other nuisance parameters are significantly pulled or constrained relative to their pre-fit values in all the background-only fits.

Table 3: Expected and observed yields in the Drell-Yan and VBF signal regions. The yields and uncertainties are presented after the background-only fit to the data in the Drell-Yan or VBF signal regions, respectively. The uncertainty in the total background estimate is smaller than the sum in quadrature of the individual background contributions due to anti-correlations between the estimates of different background sources.

	Drell-Yan signal region	VBF signal region
WZ-QCD	1733 ± 77	29 ± 4
WZ-EWK	89 ± 10	26 ± 3
$VVV + t\bar{t}V$	148 ± 27	0.9 ± 0.2
ZZ	95 ± 5	5 ± 1
Fakes/non-prompt leptons	88 ± 49	0.3 ± 0.8
Total background	2154 ± 71	61 ± 6
Observed	2155	66

The post-fit distributions of the signal regions and their respective WZ-QCD and ZZ control regions are shown in Figure 4 for the Drell-Yan selection and in Figure 5 for the VBF selection. The bottom panels show the good agreement found between the observed mass distributions and the estimated post-fit background contributions in all signal and control regions.

The largest observed excess is in the VBF category at $m(WZ)$ around 375 GeV, as shown in Figure 5(c). The local significances for VBF produced signals of a charged Higgs boson $H_5^\pm$ or a HVT W' boson are, respectively, 2.8 and 2.5 standard deviations. The respective global significances calculated using the Look Elsewhere Effect as in Ref. [100], and evaluated up to a mass of 1.2 TeV, are 1.6 and 1.7 standard deviations. In the Drell-Yan signal region the largest difference between the data and the SM background prediction is located around a mass of 1.1 TeV with a local significance of 1.2 standard deviations.

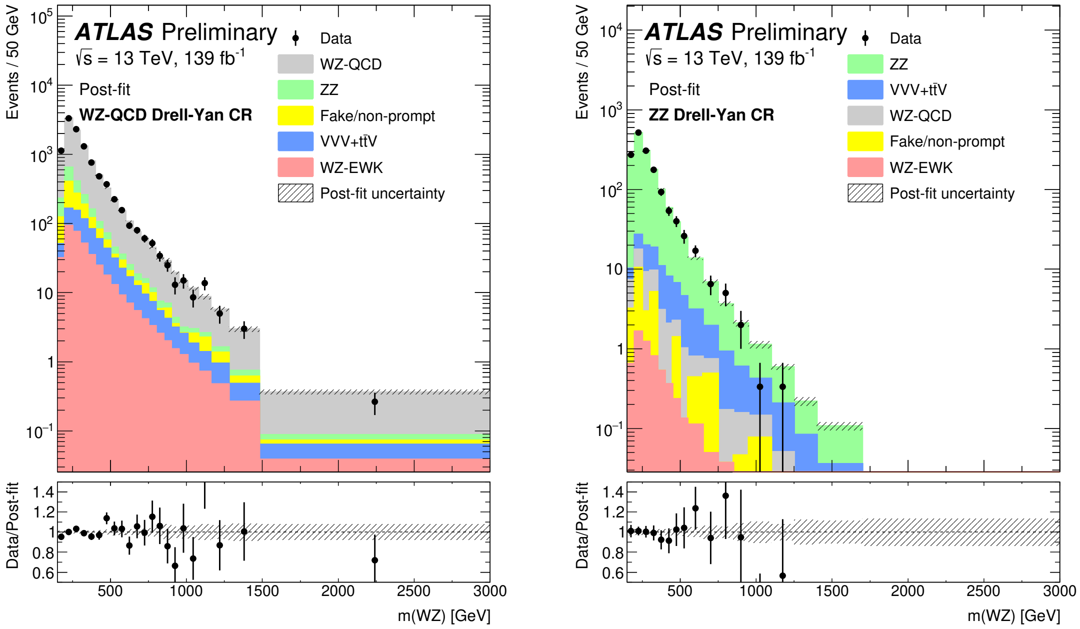

(a) *WZ*-QCD Drell-Yan control region

(b) *ZZ* Drell-Yan control region

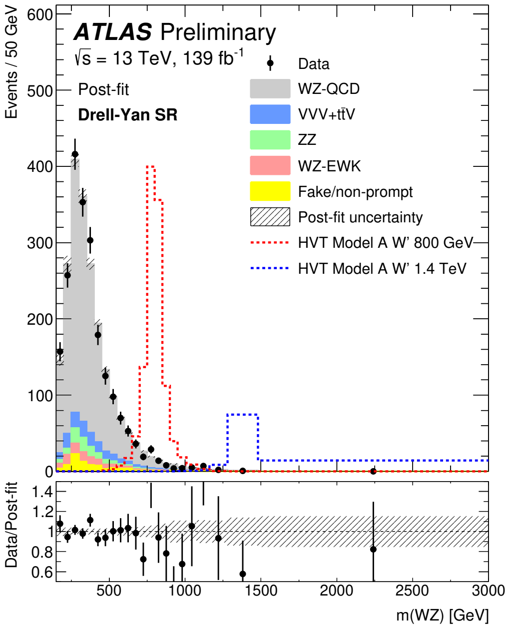

(c) Drell-Yan signal region

Figure 4: Comparisons of the data and the expected background distributions of the *WZ* invariant mass in the Drell-Yan signal region and its respective *WZ*-QCD and *ZZ* control regions. The background predictions are obtained through a background-only simultaneous fit to the Drell-Yan signal region and the *WZ*-QCD Drell-Yan and *ZZ* Drell-Yan control regions. For illustration, the expected distribution from an HVT W' resonance with mass of 800 GeV and 1.4 TeV, normalized to their predicted cross section, are shown in the signal region. The bottom panels show the ratios of the data to the post-fit background predictions. The uncertainty in the total background prediction, shown as grey bands, combines statistical and systematic contributions.

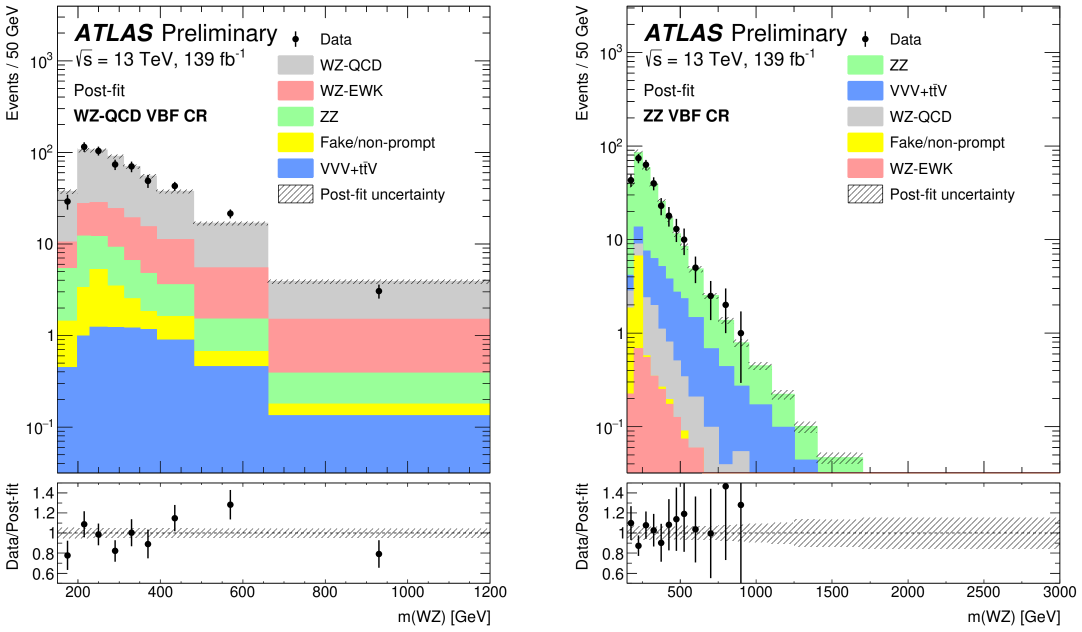

(a) *WZ*-QCD VBF control region

(b) *ZZ* VBF control region

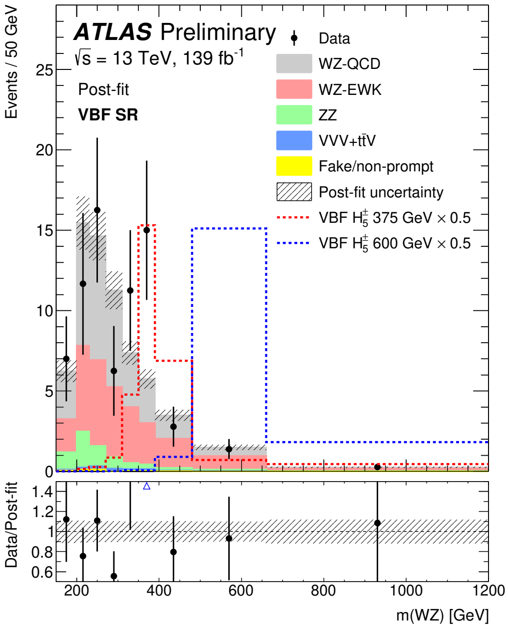

(c) VBF signal region

Figure 5: Comparisons of the data and the expected background distributions of the *WZ* invariant mass in the VBF signal region and its respective *WZ*-QCD and *ZZ* control regions. The background predictions are obtained through a background-only simultaneous fit to the VBF signal region and the *WZ*-QCD and *ZZ* VBF control regions. For illustration, the expected distribution from an $H_5^{\pm}$ GM model resonance with mass of 375 GeV and 600 GeV shown in the signal region, the signals predicted cross sections are scaled by 0.5 for presentation purposes. The bottom panels show the ratios of the data to the post-fit background predictions. The uncertainty in the total background prediction, shown as grey bands, combines statistical and systematic contributions.

8.3 Impact of systematic uncertainties

The effects of systematic uncertainties on the search are studied for hypothesised signals using the signal-strength parameter μ, which is the ratio of the extracted cross-section to the injected hypothesised signal cross-section. For this study, the signal production cross-section is set to be equal to the expected median upper limits (Section 8.4). The expected relative uncertainties in the best-fit μ value after the maximum-likelihood fit are shown in Table 4 for two reference models and mass points, for the Drell-Yan production a W' boson in the HVT model with mass $m(W')$ = 1100 GeV and for the VBF production of a $H_5^\pm$ in the GM model with mass $m(H_5^\pm)$ = 375 GeV. The individual sources of systematic uncertainty are combined into fewer background modelling and experimental categories. For signals with higher mass, the data statistical uncertainty are dominant. The uncertainties with the largest impact on the sensitivity of the searches are from the normalization of the irreducible backgrounds WZ-QCD and ZZ, from the theory modelling of the WZ background (in the table including QCD and EWK components), from the reducible background shape and normalization, and from the sizes of the MC samples. Uncertainties related to luminosity and pileup also play a relevant role in both signal regions. The jet uncertainties, such as jet energy scale and resolution, naturally have a large impact in the VBF search.

Table 4: Dominant relative uncertainties in the best-fit signal-strength parameter (μ) for a hypothetical HVT signal of mass $m(W')$ = 1 100 GeV in the Drell-Yan signal region and a GM signal of mass $m(H_5^\pm)$ = 375 GeV in the VBF signal region. For this study, the production cross-section of the signals is set to the expected median upper limits at these two mass values. Uncertainties with smaller contributions are not included.

Source of uncertainty	$\Delta\mu/\mu$ [%]	
	Drell-Yan signal region $m(W')$ = 1100 GeV	VBF signal region $m(H_5^\pm)$ = 375 GeV
WZ-QCD+ZZ normalization	2	11
WZ background: parton shower	6	1
WZ background: scale, PDF	5	8
Fake/non-prompt background	3	1
ZZ background: scale, PDF	0.2	<0.1
$VVV + t\bar{t}V$ modelling	3	1
Electron identification	6	3
Muon identification	1	4
Jet uncertainty	0.8	16
Flavour tagging	0	1
Missing transverse energy	0.2	0.5
MC statistical uncertainty	10	5
Luminosity	2	8
Pileup	0.1	8
Total systematic uncertainty	16	22
Data statistical uncertainty	54	55
Total	56	59

8.4 Limits on the production of heavy resonances

Constraints on the production of heavy resonances are derived by repeating the fit to the signal-plus-background hypothesis for different signal models. Upper limits on cross-sections times branching fraction to WZ are calculated using the asymptotic approximation [98].

For the HVT model search, Figure 6 presents the observed and expected limits on $\sigma \times B(W' \to WZ)$ at 95% CL as a function of the W' mass for the HVT model in the Drell-Yan signal region. Masses below 2.4 TeV can be excluded for Model A and 2.5 TeV for Model B. For resonance masses above 2 TeV the exclusion limits become worse due to the poorer acceptance at high mass (see Figure 1). Regarding the VBF production mode, the limit on $\sigma \times B(W' \to WZ)$ is shown in Figure 7. Masses below 340 GeV, 500 GeV and 700 GeV can be excluded for the HVT VBF model with $c_F = 0$ and $g_V c_H = 1.0$, 1.5 and 2.0, respectively.

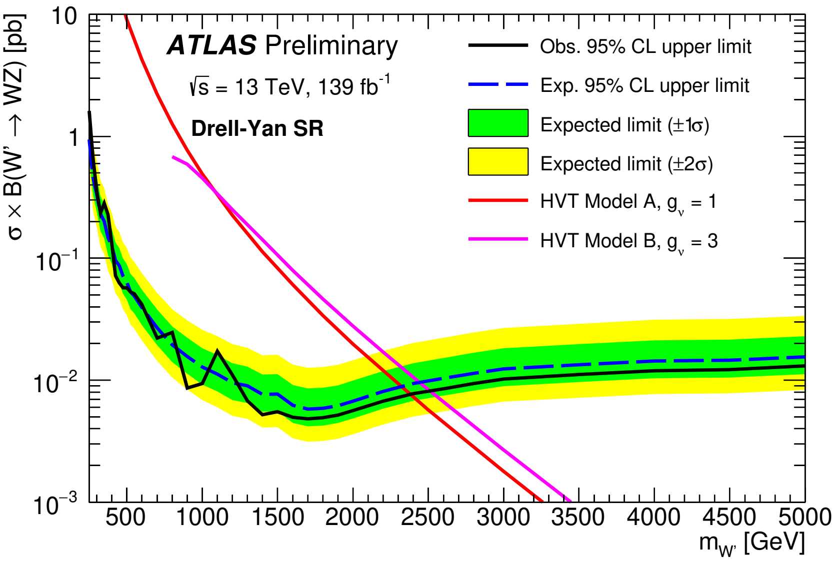

Figure 6: Observed and expected 95% CL exclusion upper limits on $\sigma \times B(W' \to WZ)$ for the Drell-Yan production of a W' boson in the HVT model as a function of its mass. The LO theory predictions for HVT Model A with $g_V = 1$ and Model B with $g_V = 3$ are also shown.

For the $H_5^{\pm}$ GM search, observed and expected exclusion limits at 95% confidence level (CL) on $\sigma \times B(H_5^{\pm} \to WZ)$ and on the mixing parameter $\sin\theta_H$ are shown in in Figure 8. The intrinsic width of the scalar resonance, for $\sin\theta_H = 0.5$, is narrower than the detector resolution in the mass region explored. The shaded regions show the parameter space for which the $H_5^{\pm}$ width exceeds 5% and 10% of $m_{H_5^{\pm}}$.

As a test of the asymptotic approximation used in the statistical analysis, limits are also computed with ensembles of pseudoexperiments in all signal and control regions. The cross-section upper limits obtained in that case agree in all cases for masses below 500 GeV. At higher masses, where event yields become smaller and smaller, the discrepancy between the two methods become larger, but they remain within 6-10%.

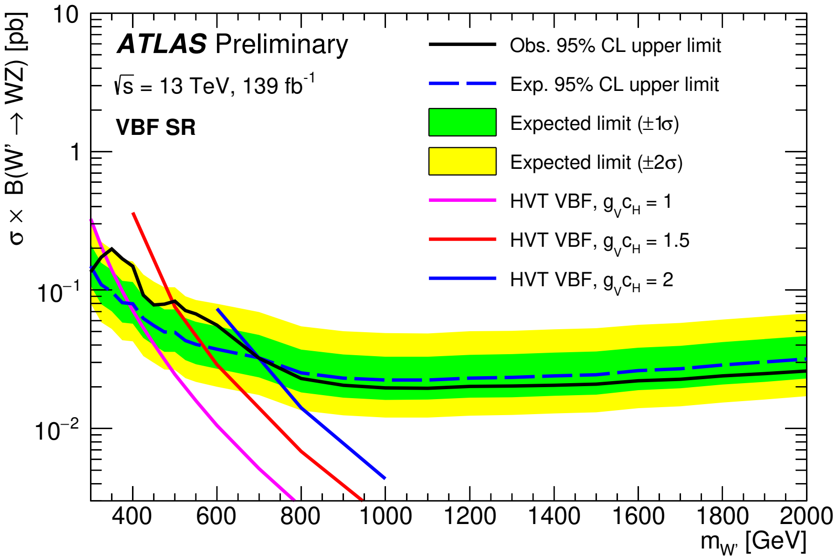

Figure 7: Observed and expected 95% CL upper limits on $\sigma \times B(W' \rightarrow WZ)$ for the VBF production of a W' boson in the HVT with parameter $c_F = 0$, as a function of its mass. The LO theory predictions for HVT VBF model with different values of the coupling parameters g_V and c_H are also shown.

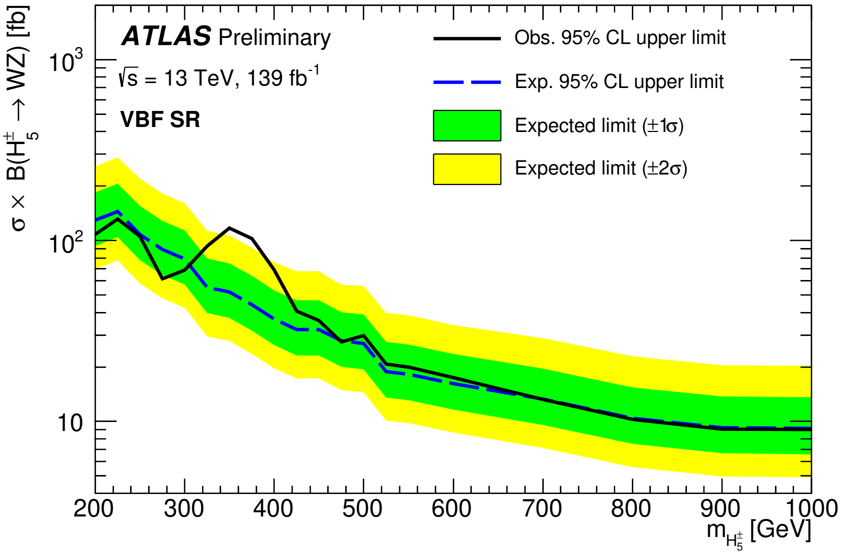

(a)

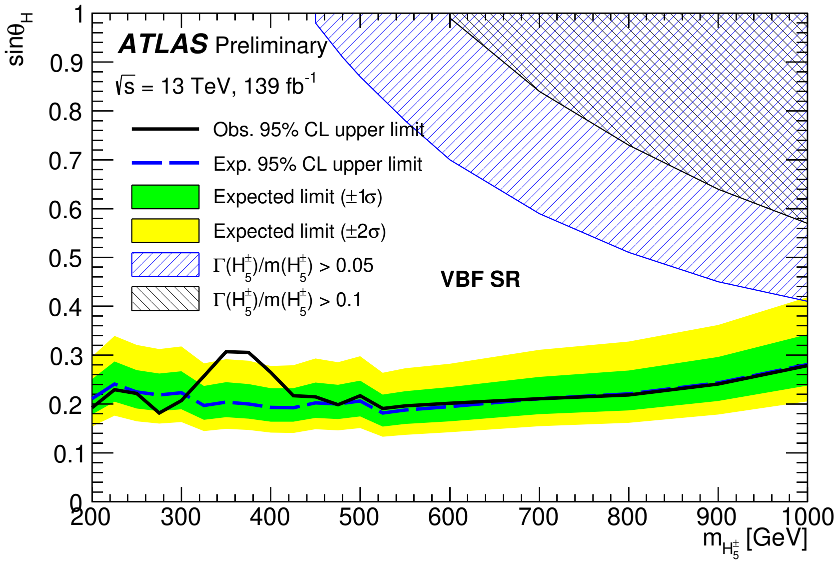

(b)

Figure 8: Observed and expected 95% CL upper limits (a) on $\sigma \times B(H_5^\pm \to WZ)$ and (b) on the parameter $\sin\theta_H$ of the GM model as a function of $m_{H_5^\pm}$. The shaded region shows where the theoretical intrinsic width of the resonance would be larger than 5% or 10% of the mass.

9 Conclusions

A search was performed for resonant WZ production in the fully leptonic final states (electrons and muons) using pp collision data collected by the ATLAS experiment at $\sqrt{s} = 13$ TeV with an integrated luminosity of 139 fb^{-1}. Two different production processes are considered, Drell-Yan and vector-boson fusion.

The data in the Drell-Yan selection are found to be consistent with Standard Model predictions. The results are used to derive upper limits at 95% confidence level on the cross-section times branching ratio of the phenomenological Heavy Vector Triplet benchmark Model A (Model B) with coupling constant $g_V = 1$ ($g_V = 3$) as a function of the resonance mass, with no evidence of heavy vector resonance production for masses below 2.4 (2.5) TeV.

In the case of the VBF production process, limits on the production cross-section times branching ratio to WZ of a hypothetical resonance are obtained as a function of the mass for a heavy vector triplet or for a charged member of the fiveplet scalar in the Georgi–Machacek model. The results show a local excess of events over the Standard Model expectations at a resonance mass of around 375 GeV. The local significances for signals of a heavy vector W' boson or a $H_5^{\pm}$ are 2.5 and 2.8 standard deviations respectively. The respective global significances calculated considering the Look Elsewhere effect are 1.7 and 1.6 standard deviations respectively. With no evidence of heavy vector W' resonance production, masses below 340 GeV, 500 GeV and 700 GeV for HVT VBF production can be excluded for a model with $g_V c_H$ parameters product set to 1.0, 1.5 and 2.0, respectively.

References

[1] D. de Florian et al., *Handbook of LHC Higgs Cross Sections: 4. Deciphering the Nature of the Higgs Sector*, **2/2017** (2016), arXiv: `1610.07922 [hep-ph]`.

[2] I. P. Ivanov, *Building and testing models with extended Higgs sectors*, Prog. Part. Nucl. Phys. **95** (2017) 160, arXiv: `1702.03776 [hep-ph]`.

[3] J. Steggemann, *Extended Scalar Sectors*, Ann. Rev. Nucl. Part. Sci. **70** (2020) 197.

[4] P. Langacker, R. W. Robinett and J. L. Rosner, *New Heavy Gauge Bosons in pp and $p\bar{p}$ Collisions*, Phys. Rev. D **30** (1984) 1470.

[5] G. Altarelli, B. Mele and M. Ruiz-Altaba, *Searching for New Heavy Vector Bosons in $p\bar{p}$ Colliders*, Z. Phys. C **45** (1989) 109.

[6] K. Agashe, R. Contino and A. Pomarol, *The minimal composite Higgs model*, Nucl.Phys. B **719** (2005) 165, arXiv: `hep-ph/0412089 [hep-ph]`.

[7] G. Giudice, C. Grojean, A. Pomarol and R. Rattazzi, *The strongly-interacting light Higgs*, JHEP **06** (2007) 045, arXiv: `hep-ph/0703164 [hep-ph]`.

[8] R. Foadi, M. T. Frandsen, T. A. Ryttov and F. Sannino, *Minimal Walking Technicolor: Set Up for Collider Physics*, Phys. Rev. D **76** (2007) 055005, arXiv: `0706.1696 [hep-ph]`.

[9] L. Randall and R. Sundrum, *A large mass hierarchy from a small extra dimension*, Phys. Rev. Lett. **83** (1999) 3370, arXiv: `hep-ph/9905221`.

[10] C. Csaki, C. Grojean, H. Murayama, L. Pilo and J. Terning, *Gauge theories on an interval: Unitarity without a Higgs*, Phys. Rev. D **69** (2004) 055006, arXiv: `hep-ph/0305237 [hep-ph]`.

[11] ATLAS Collaboration, *The ATLAS Experiment at the CERN Large Hadron Collider*, JINST **3** (2008) S08003.

[12] A. Djouadi, *The Anatomy of electro-weak symmetry breaking. II. The Higgs bosons in the minimal supersymmetric model*, Phys. Rept. **459** (2008) 1, arXiv: `hep-ph/0503173`.

[13] R. N. Mohapatra and J. C. Pati, *Left-right gauge symmetry and an "isoconjugate" model of CP violation*, Phys. Rev. D **11** (1975) 566.

[14] N. Arkani-Hamed, A. G. Cohen, E. Katz and A. E. Nelson, *The Littlest Higgs*, JHEP **07** (2002) 034, arXiv: `hep-ph/0206021`.

[15] T. Han, H. E. Logan, B. McElrath and L.-T. Wang, *Phenomenology of the little Higgs model*, Phys. Rev. D **67** (2003) 095004, arXiv: `hep-ph/0301040`.

[16] H. Georgi and M. Machacek, *Doubly charged Higgs bosons*, Nucl. Phys. B **262** (1985) 463.

[17] M. S. Chanowitz and M. Golden, *Higgs boson triplets with $M(W) = M(Z) \cos\theta_W$*, Phys. Lett. B **165** (1985) 105.

[18] K. Hartling, K. Kumar and H. E. Logan, *Indirect constraints on the Georgi-Machacek model and implications for Higgs boson couplings*, Phys. Rev. D **91** (2015) 015013, arXiv: `1410.5538 [hep-ph]`.

[19] J. de Blas, J. M. Lizana and M. Perez-Victoria, *Combining searches of Z' and W' bosons*, JHEP **01** (2013) 166, arXiv: `1211.2229 [hep-ph]`.

[20] D. Pappadopulo, A. Thamm, R. Torre and A. Wulzer, *Heavy vector triplets: bridging theory and data*, JHEP **09** (2014) 060, arXiv: `1402.4431 [hep-ph]`.

[21] D. Greco and D. Liu, *Hunting composite vector resonances at the LHC: naturalness facing data*, JHEP **12** (2014) 126, arXiv: `1410.2883 [hep-ph]`.

[22] M. S. Chanowitz and M. K. Gaillard, *The TeV Physics of Strongly Interacting W's and Z's*, Nucl. Phys. B **261** (1985) 379.

[23] ATLAS Collaboration, *Search for WZ resonances in the fully leptonic channel using pp collisions at $\sqrt{s} = 8$ TeV with the ATLAS detector*, Phys. Lett. B **737** (2014) 223, arXiv: `1406.4456 [hep-ex]`.

[24] ATLAS Collaboration, *Search for resonant WZ production in the fully leptonic final state in proton–proton collisions at $\sqrt{s} = 13$ TeV with the ATLAS detector*, Phys. Lett. B **787** (2018) 68, arXiv: `1806.01532 [hep-ex]`.

[25] CMS Collaboration, *Search for charged Higgs bosons produced in vector boson fusion processes and decaying into vector boson pairs in proton–proton collisions at $\sqrt{s} = 13$ TeV*, Eur. Phys. J. C **81** (2021) 723, arXiv: `2104.04762 [hep-ex]`.

[26] ATLAS Collaboration, *ATLAS Heavy Particle Searches - 95% CL Exclusion Limits*, 2021, URL: `https://atlas.web.cern.ch/Atlas/GROUPS/PHYSICS/PUBNOTES/ATL-PHYS-PUB-2021-033/fig_01.png`.

[27] ATLAS Collaboration, *Summary of Diboson Resonance Searches from the ATLAS Experiment*, ATL-PHYS-PUB-2021-018, 2021, URL: `https://cds.cern.ch/record/2771783`.

[28] CMS Collaboration, *Overview of CMS EXO results*, 2021, URL: `https://twiki.cern.ch/twiki/pub/CMSPublic/SummaryPlotsEXO13TeV/CurrentBarChartVersion_v7.svg`.

[29] ATLAS Collaboration, *Combination of searches for WW, WZ, and ZZ resonances in pp collisions at $\sqrt{s} = 8$ TeV with the ATLAS detector*, Phys. Lett. B **755** (2016) 285, arXiv: `1512.05099 [hep-ex]`.

[30] ATLAS Collaboration, *Searches for heavy diboson resonances in pp collisions at $\sqrt{s} = 13$ TeV with the ATLAS detector*, JHEP **09** (2016) 173, arXiv: `1606.04833 [hep-ex]`.

[31] ATLAS Collaboration, *Search for heavy diboson resonances in semileptonic final states in pp collisions at $\sqrt{s} = 13$ TeV with the ATLAS detector*, Eur. Phys. J. C **80** (2020) 1165, arXiv: `2004.14636 [hep-ex]`.

[32] CMS Collaboration, *Combination of searches for heavy resonances decaying to WW, WZ, ZZ, WH, and ZH boson pairs in proton–proton collisions at $\sqrt{s} = 8$ TeV and 13 TeV*, Phys. Lett. B **774** (2017) 533, arXiv: `1705.09171 [hep-ex]`.

[33] CMS Collaboration, *Observation of Electroweak Production of Same-Sign W Boson Pairs in the Two Jet and Two Same-Sign Lepton Final State in Proton–Proton Collisions at 13 TeV*, Phys. Rev. Lett. **120** (2018) 081801, arXiv: `1709.05822 [hep-ex]`.

[34] ATLAS Collaboration, *Search for heavy resonances decaying into WW in the $e\nu\mu\nu$ final state in pp collisions at $\sqrt{s} = 13$ TeV with the ATLAS detector*, Eur. Phys. J. C **78** (2018) 24, arXiv: `1710.01123 [hep-ex]`.

[35] ATLAS Collaboration, *Performance of the ATLAS trigger system in 2015*, Eur. Phys. J. C **77** (2017) 317, arXiv: `1611.09661 [hep-ex]`.

[36] ATLAS Collaboration, *The ATLAS Collaboration Software and Firmware*, ATL-SOFT-PUB-2021-001, 2021, URL: `https://cds.cern.ch/record/2767187`.

[37] ATLAS Collaboration, *ATLAS data quality operations and performance for 2015–2018 data-taking*, JINST **15** (2020) P04003, arXiv: `1911.04632 [physics.ins-det]`.

[38] ATLAS Collaboration, *Performance of electron and photon triggers in ATLAS during LHC Run 2*, Eur. Phys. J. C **80** (2020) 47, arXiv: `1909.00761 [hep-ex]`.

[39] ATLAS Collaboration, *Performance of the ATLAS muon triggers in Run 2*, JINST **15** (2020) P09015, arXiv: `2004.13447 [hep-ex]`.

[40] S. Agostinelli et al., *GEANT4: A simulation toolkit*, Nucl. Instrum. Meth. A **506** (2003) 250.

[41] ATLAS Collaboration, *The ATLAS Simulation Infrastructure*, Eur. Phys. J. C **70** (2010) 823, arXiv: `1005.4568 [physics.ins-det]`.

[42] ATLAS Collaboration, *The simulation principle and performance of the ATLAS fast calorimeter simulation FastCaloSim*, ATL-PHYS-PUB-2010-013, 2010, URL: `https://cds.cern.ch/record/1300517`.

[43] T. Sjöstrand, S. Mrenna and P. Z. Skands, *A brief introduction to PYTHIA 8.1*, Comput. Phys. Commun. **178** (2008) 852, arXiv: `0710.3820 [hep-ph]`.

[44] R. D. Ball et al., *Parton distributions with LHC data*, Nucl. Phys. B **867** (2013) 244, arXiv: `1207.1303 [hep-ph]`.

[45] ATLAS Collaboration, *The Pythia 8 A3 tune description of ATLAS minimum bias and inelastic measurements incorporating the Donnachie–Landshoff diffractive model*, ATL-PHYS-PUB-2016-017, 2016, URL: `https://cds.cern.ch/record/2206965`.

[46] T. Gleisberg et al., *Event generation with SHERPA 1.1*, JHEP **02** (2009) 007, arXiv: `0811.4622 [hep-ph]`.

[47] D. J. Lange, *The EvtGen particle decay simulation package*, Nucl. Instrum. Meth. A **462** (2001) 152.

[48] J. Alwall et al., *The automated computation of tree-level and next-to-leading order differential cross sections, and their matching to parton shower simulations*, JHEP **07** (2014) 079, arXiv: `1405.0301 [hep-ph]`.

[49] C. Degrande, K. Hartling, H. E. Logan, A. D. Peterson and M. Zaro, *Automatic predictions in the Georgi-Machacek model at next-to-leading order accuracy*, Phys. Rev. **D93** (2016) 035004, arXiv: `1512.01243 [hep-ph]`.

[50] H. E. Logan and M. B. Reimer, *Characterizing a benchmark scenario for heavy Higgs boson searches in the Georgi-Machacek model*, Phys. Rev. D **96** (2017) 095029, arXiv: `1709.01883 [hep-ph]`.

[51] K. Hartling, K. Kumar and H. E. Logan, *GMCALC: a calculator for the Georgi-Machacek model*, (2014), arXiv: `1412.7387 [hep-ph]`.

[52] R. D. Ball et al., *Parton distributions for the LHC run II*, JHEP **04** (2015) 040, arXiv: `1410.8849 [hep-ph]`.

[53] ATLAS Collaboration, *ATLAS Pythia 8 tunes to 7 TeV data*, ATL-PHYS-PUB-2014-021, 2014, URL: `https://cds.cern.ch/record/1966419`.

[54] A. Ballestrero et al., *Precise predictions for same-sign W-boson scattering at the LHC*, Eur. Phys. J. C **78** (2018) 671, arXiv: `1803.07943 [hep-ph]`.

[55] V. D. Barger, W.-Y. Keung and E. Ma, *A gauge model with light W and Z bosons*, Phys. Rev. D **22** (1980) 727.

[56] R. Contino, D. Marzocca, D. Pappadopulo and R. Rattazzi, *On the effect of resonances in composite Higgs phenomenology*, JHEP **10** (2011) 081, arXiv: `1109.1570 [hep-ph]`.

[57] R. Frederix and S. Frixione, *Merging meets matching in MC@NLO*, JHEP **12** (2012) 061, arXiv: `1209.6215 [hep-ph]`.

[58] E. Bothmann et al., *Event generation with Sherpa 2.2*, SciPost Phys. **7** (2019) 034, arXiv: `1905.09127 [hep-ph]`.

[59] T. Gleisberg and S. Höche, *Comix, a new matrix element generator*, JHEP **12** (2008) 039, arXiv: `0808.3674 [hep-ph]`.

[60] S. Schumann and F. Krauss, *A parton shower algorithm based on Catani–Seymour dipole factorisation*, JHEP **03** (2008) 038, arXiv: `0709.1027 [hep-ph]`.

[61] S. Höche, F. Krauss, M. Schönherr and F. Siegert,
A critical appraisal of NLO+PS matching methods, JHEP **09** (2012) 049,
arXiv: `1111.1220 [hep-ph]`.

[62] S. Höche, F. Krauss, M. Schönherr and F. Siegert,
QCD matrix elements + parton showers. The NLO case, JHEP **04** (2013) 027,
arXiv: `1207.5030 [hep-ph]`.

[63] S. Catani, F. Krauss, R. Kuhn and B. R. Webber, *QCD Matrix Elements + Parton Showers*,
JHEP **11** (2001) 063, arXiv: `hep-ph/0109231`.

[64] S. Höche, F. Krauss, S. Schumann and F. Siegert, *QCD matrix elements and truncated showers*,
JHEP **05** (2009) 053, arXiv: `0903.1219 [hep-ph]`.

[65] T. Sjöstrand et al., *An introduction to PYTHIA 8.2*, Comput. Phys. Commun. **191** (2015) 159,
arXiv: `1410.3012 [hep-ph]`.

[66] P. Nason, *A new method for combining NLO QCD with shower Monte Carlo algorithms*,
JHEP **11** (2004) 040, arXiv: `hep-ph/0409146`.

[67] S. Frixione, P. Nason and C. Oleari,
Matching NLO QCD computations with parton shower simulations: the POWHEG method,
JHEP **11** (2007) 070, arXiv: `0709.2092 [hep-ph]`.

[68] S. Alioli, P. Nason, C. Oleari and E. Re, *A general framework for implementing NLO calculations in shower Monte Carlo programs: the POWHEG BOX*, JHEP **06** (2010) 043,
arXiv: `1002.2581 [hep-ph]`.

[69] S. Alioli, P. Nason, C. Oleari and E. Re,
NLO vector-boson production matched with shower in POWHEG, JHEP **07** (2008) 060,
arXiv: `0805.4802 [hep-ph]`.

[70] ATLAS Collaboration, *Measurement of the Z/γ^* boson transverse momentum distribution in pp collisions at $\sqrt{s} = 7$ TeV with the ATLAS detector*, JHEP **09** (2014) 145,
arXiv: `1406.3660 [hep-ex]`.

[71] H.-L. Lai et al., *New parton distributions for collider physics*, Phys. Rev. D **82** (2010) 074024,
arXiv: `1007.2241 [hep-ph]`.

[72] J. Pumplin et al.,
New Generation of Parton Distributions with Uncertainties from Global QCD Analysis,
JHEP **07** (2002) 012, arXiv: `hep-ph/0201195`.

[73] P. Golonka and Z. Was,
PHOTOS Monte Carlo: a precision tool for QED corrections in Z and W decays,
Eur. Phys. J. C **45** (2006) 97, arXiv: `hep-ph/0506026`.

[74] N. Davidson, T. Przedzinski and Z. Was,
PHOTOS Interface in C++: Technical and physics documentation,
Comput. Phys. Commun. **199** (2016) 86, arXiv: `1011.0937 [hep-ph]`.

[75] S. Alioli, P. Nason, C. Oleari and E. Re,
NLO single-top production matched with shower in POWHEG: s- and t-channel contributions,
JHEP **09** (2009) 111, arXiv: `0907.4076 [hep-ph]`, Erratum: JHEP **02** (2010) 011.

[76] ATLAS Collaboration, *Electron and photon performance measurements with the ATLAS detector using the 2015–2017 LHC proton–proton collision data*, JINST **14** (2019) P12006,
arXiv: `1908.00005 [hep-ex]`.

[77] ATLAS Collaboration, *Muon reconstruction performance of the ATLAS detector in proton–proton collision data at* $\sqrt{s} = 13$ *TeV*, Eur. Phys. J. C **76** (2016) 292, arXiv: `1603.05598 [hep-ex]`.

[78] ATLAS Collaboration,
Jet reconstruction and performance using particle flow with the ATLAS Detector,
Eur. Phys. J. C **77** (2017) 466, arXiv: `1703.10485 [hep-ex]`.

[79] M. Cacciari, G. P. Salam and G. Soyez, *The anti-*k_t *jet clustering algorithm*, JHEP **04** (2008) 063, arXiv: `0802.1189 [hep-ph]`.

[80] M. Cacciari, G. P. Salam and G. Soyez, *FastJet user manual*, Eur. Phys. J. C **72** (2012) 1896, arXiv: `1111.6097 [hep-ph]`.

[81] ATLAS Collaboration, *Performance of pile-up mitigation techniques for jets in* pp *collisions at* $\sqrt{s} = 8$ *TeV using the ATLAS detector*, Eur. Phys. J. C **76** (2016) 581,
arXiv: `1510.03823 [hep-ex]`.

[82] ATLAS Collaboration, *Tagging and suppression of pileup jets with the ATLAS detector*, ATLAS-CONF-2014-018, 2014, URL: `https://cds.cern.ch/record/1700870`.

[83] ATLAS Collaboration, *ATLAS b-jet identification performance and efficiency measurement with* $t\bar{t}$ *events in* pp *collisions at* $\sqrt{s} = 13$ *TeV*, Eur. Phys. J. C **79** (2019) 970,
arXiv: `1907.05120 [hep-ex]`.

[84] ATLAS Collaboration, *Measurement of the b-jet identification efficiency for high transverse momentum jets in* $t\bar{t}$ *events in the lepton + jets channel with the ATLAS detector using Run 2 data*, (2021), URL: `https://cds.cern.ch/record/2753734`.

[85] ATLAS Collaboration, *Performance of missing transverse momentum reconstruction with the ATLAS detector using proton–proton collisions at* $\sqrt{s} = 13$ *TeV*, Eur. Phys. J. C **78** (2018) 903, arXiv: `1802.08168 [hep-ex]`.

[86] F. Chollet et al., *Keras*, 2015, URL: `https://github.com/fchollet/keras`.

[87] Martín Abadi et al., *TensorFlow: Large-Scale Machine Learning on Heterogeneous Systems*, Software available from tensorflow.org, 2015, URL: `https://www.tensorflow.org/`.

[88] I. Sutskever, J. Martens, G. Dahl and G. Hinton,
'On the importance of initialization and momentum in deep learning',
Proceedings of the 30th International Conference on Machine Learning,
ed. by S. Dasgupta and D. McAllester, vol. 28, Proceedings of Machine Learning Research 3,
Atlanta, Georgia, USA: PMLR, 2013 1139.

[89] ATLAS Collaboration, *Measurements of* $W^{\pm}Z$ *production cross sections in* pp *collisions at* $\sqrt{s} = 8$ *TeV with the ATLAS detector and limits on anomalous gauge boson self-couplings*, Phys. Rev. D **93** (2016) 092004, arXiv: `1603.02151 [hep-ex]`.

[90] J. Butterworth et al., *PDF4LHC recommendations for LHC Run II*, J. Phys. G **43** (2016) 023001, arXiv: `1510.03865 [hep-ph]`.

[91] ATLAS Collaboration, *Multi-boson simulation for* 13 *TeV ATLAS analyses*,
ATL-PHYS-PUB-2016-002, 2016, URL: `https://cds.cern.ch/record/2119986`.

[92] ATLAS Collaboration, *Measurement of the* $t\bar{t}Z$ *and* $t\bar{t}W$ *cross sections in proton–proton collisions at* $\sqrt{s} = 13$ *TeV with the ATLAS detector*, Phys. Rev. D **99** (2019) 072009,
arXiv: `1901.03584 [hep-ex]`.

[93] ATLAS Collaboration,
Evidence for the production of three massive vector bosons with the ATLAS detector,
Phys. Lett. B **798** (2019) 134913, arXiv: `1903.10415 [hep-ex]`.

[94] ATLAS Collaboration,
Luminosity determination in pp collisions at $\sqrt{s} = 13$ TeV using the ATLAS detector at the LHC,
ATLAS-CONF-2019-021, 2019, URL: `https://cds.cern.ch/record/2677054`.

[95] G. Avoni et al., *The new LUCID-2 detector for luminosity measurement and monitoring in ATLAS*,
JINST **13** (2018) P07017.

[96] ATLAS Collaboration, *Measurement of the Inelastic Proton–Proton Cross Section at $\sqrt{s} = 13$ TeV with the ATLAS Detector at the LHC*, Phys. Rev. Lett. **117** (2016) 182002,
arXiv: `1606.02625 [hep-ex]`.

[97] ATLAS Collaboration, *Jet energy scale measurements and their systematic uncertainties in proton–proton collisions at $\sqrt{s} = 13$ TeV with the ATLAS detector*, Phys. Rev. D **96** (2017) 072002,
arXiv: `1703.09665 [hep-ex]`.

[98] G. Cowan, K. Cranmer, E. Gross and O. Vitells,
Asymptotic formulae for likelihood-based tests of new physics, Eur. Phys. J. C **71** (2011) 1554,
arXiv: `1007.1727 [physics.data-an]`, Erratum: Eur. Phys. J. C **73** (2013) 2501.

[99] A. L. Read, *Presentation of search results: the CL_S technique*, J. Phys. G **28** (2002) 2693.

[100] ATLAS Collaboration, *Procedure for the LHC Higgs boson search combination in summer 2011*,
ATL-PHYS-PUB-2011-011, 2011, URL: `https://cds.cern.ch/record/1375842`.